Metrics for next-generation gravitational-wave detectors

Evan D. Hall[1] and Matthew Evans[1]

[1]*LIGO Laboratory, Massachusetts Institute of Technology, Cambridge, MA 02139, USA*

Abstract

I. INTRODUCTION

Gravitational-wave science, which started in earnest with the first detection of gravitational-waves in 2015 [1], has immense unexplored potential. Aiming to exploit this potential, the next generation of detectors is being designed [2, 3] and plans for their construction are taking shape. It is clear that to get the most science out of the gravitational-wave signals we detect, a network of large-scale observatories will be required. At present there are many unanswered questions about how best to construct such a network.

In this paper, we will address several of the fundamental questions required to maximize the scientific potential of a terrestrial gravitational-wave detector network. These questions include: Which science goals are sensitive to the location and orientation of the detectors in the network? How the does design of the network's constituents impact its output? What science can be done with a heterogeneous mix of second and third generation detectors?

In the past, "optimizing the science" from gravitational-wave astronomy has been less of an exercise in network optimization and more an exercise in optimizing the performance of single detectors, as measured via metrics such as the "inspiral range"—the distance (or redshift) out to which each detector could detect a model system (usually a 1.4–1.4 $M_\odot$ binary coalescence) with a certain signal-to-noise ratio cite—or the detector's strain sensitivity [4]. Modern examples of these single-detector metrics are given in Fig. 1 and Fig. 2.

There are early examples of what could be called network optimization, such as the decision to coalign the Hanford and Livingston facilities to maximize coincident detections and the longstanding desire to have at least three widely separated facilities in order to triangulate source positions on the sky. However, systematic studies of gravitational-wave detector network optimization, measured quantitatively via a set of metrics, are relatively recent. Raffai et al. [5] optimized the facility placement of a set of triangular (Einstein-Telescope-like) detectors as well as the placement of a LIGO facility in India. This procedure was then generalized by Hu et al. [6]. Michimura et al. [7] optimized the optical configuration of the Kagra detector [8] with respect to the sky localization performance of the global advanced detector network.

More generally, others have already examined the performance of a limited number of plausible third-generation gravitational-wave networks against some set of metrics. The binary-neutron-star (BNS) localization capabilities of networks with third-generation detectors has been explored by Mills et al. [9]. The binary-black-hole (BBH) parameter estimation capabilities—including masses, spins, redshift, and localization—of networks with third-generation detectors has been explored by Vitale and Evans [10] and Vitale and Whittle [11].

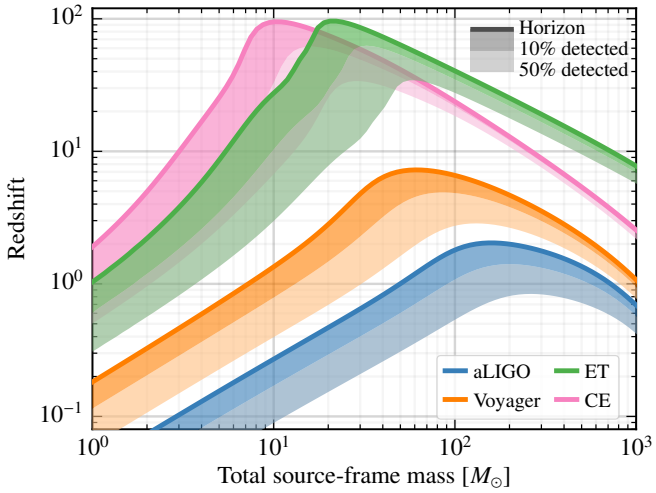

FIG. 1: Astrophysical reach [12] of selected second- and third-generation detectors for equal-mass, nonspinning binaries, shown as a function of total source-frame mass. The binaries are distributed isotropically in sky location and inclination angle. The solid lines denote the horizon—the redshift beyond which none of the sources are detected. The shaded bands then show the redshifts at which 10% and 50% of the sources would be detected. Here a source is assumed to be detected if it appears in a detector with matched-filter signal-to-noise ratio $\rho \geq 8$. The detectors considered here are Advanced LIGO (aLIGO) [13], Voyager [14], Einstein Telescope (ET) [2], and Cosmic Explorer (CE) [3]. The astrophysical reach is the cosmological generalization of various luminosity-distance measures (such as the inspiral horizon distance [15]) that have been used to characterize detector performance.

While these works evaluate the performance of some networks, and optimize a few sets of detectors for a few performance metrics, they do not address the critical questions posed earlier in this section. In our work, we present in full the performance of a large ensemble of networks against a list of metrics, in order to see the full landscape of network performance. This allows us to say not only whether an optimum exists for some particular metric, but whether the range of performance for different network realizations is large enough to even warrant optimization.

II. METRICS TO CONNECT NETWORK PARAMETERS WITH SCIENCE GOALS

The questions raised in Sec. I naturally drive one to "optimally" choose the network parameters—the number, type, location, and orientation of third-generation instruments across

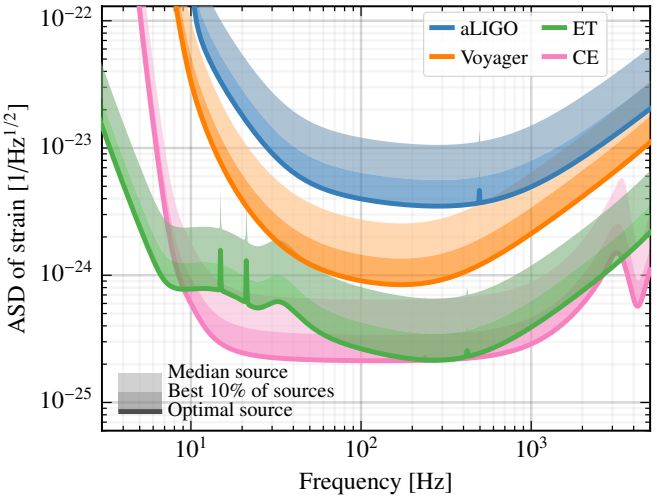

FIG. 2: Effective sensitivities of selected second- and third-generation detectors for monochromatic sources distributed isotropically in sky position, inclination, and polarization. The solid lines denote the effective strain sensitivity for an optimally oriented source. The bands then denote the effective sensitivity for the best 10% of sources, and the median source. The detectors considered here are Advanced LIGO (aLIGO), Voyager, Einstein Telescope (ET), and Cosmic Explorer (CE).

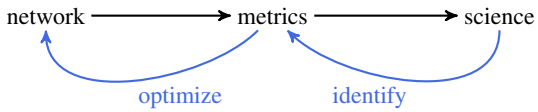

FIG. 3: Anticipated procedure for determining an optimal network configuration from a set of science goals.

the globe—based on the needs of the science goals, such as determining the history of star formation, testing corrections to general relativity, uncovering the nuclear physics inside neutron stars and supernovae, and constraining the dark energy equation of state. Each of these science goals involves a variety of data analysis techniques and scientific products whose connection to the network parameters is not immediately obvious. While one could imagine an optimization procedure that connects each network parameter (the location of a particular facility, for example) to each science goal (the dark energy equation of state, for example), such a procedure results in a set of connections that is opaque and can quickly grow to encompass a large number of variables.

For these reasons, network optimization studies [5–7] focus on optimizing a smaller number of metrics, by which we mean intermediate data products that have a reasonably clear dependence on the network parameters and which then feed into the more specialized analysis that is used to achieve the science goals. Such metrics include signal-to-noise ratio, polarization sensitivity, and source localization (see Fig. 3).

In addition to choosing a set of metrics, one must also choose what percentile to optimize for. Certain studies benefit from the large statistics of the total population of events, thereby suggesting that metrics should be optimized for the median event. Other studies benefit from collecting a few of the loudest events, thereby suggesting that metrics should be optimized for loudest events. Still other studies require collecting a few rare or special events, which may not be captured in the generic metrics; these studies may prefer to optimize the median event so as not to lose out on the rare events.

Code	Location	Lat.	Long.	θ_{XE}
H	Hanford, USA	46.5	−119.4	126
L	Livingston, USA	30.6	−90.8	−162
V	Pisa, Italy	43.6	10.5	71
I*	India	14.2	76.4	45
K	Kamioka, Japan	36.4	137.3	28
E*	Europe	47.4	8.5	11
A*	Western Australia	−31.5	118.0	−58
U*	Utah, USA	40.8	−113.8	−30

TABLE I: Coordinates and orientations for the facilities considered in this work. θ_{XE} is the counterclockwise angle from due east made by the X-arm (or for ET, by any one of the sides of the triangle). Facilities with an asterisk have not been constructed and the coordinates are chosen for illustrative purposes only.

In the following section we choose a few example metrics and explore how different third-generation networks perform. **(ME: say more about how our choices link back to science)**

III. METRICS

As illustrative examples we choose

1. the sky localization area of 1.4–1.4 $M_\odot$ binary neutron star coalescences at redshift $z = 0.3$, a metric useful for assessing the feasibility of electromagnetic followup;
2. the signal-to-noise ratio of 30–30 $M_\odot$ binary black hole coalescences at redshift $z = 2$, a metric for quantifying the quality of the most frequent events;
3. the distance uncertainty (or equivalently, redshift uncertainty) of the 30–30 $M_\odot$ binary black hole coalescences at $z = 2$, a metric useful for assessing the constraining power of third-generation networks on the stellar evolution history of the universe;
4. the inclination angle uncertainty of the same 30–30 $M_\odot$ systems at $z = 2$, which is representative of the network's ability to distinguish between gravitational-wave polarizations; and
5. the signal-to-noise ratio of a high-frequency strain signal, a metric useful for studies of the post-merger signal in neutron star coalescences.

In all cases the components of the binary are non-spinning and have equal mass. Sky locations, inclinations, and polarization angles are isotropic.

In order to assess the access of a set of gravitational-wave detectors to a given science goal, we evaluate each of the above example metrics for an ensemble of networks composed of the set of detectors under consideration. For example, a network composed of one evolved second-generation detector and two third-generation detectors (e.g., the Voyager, ET and

Network	H	L	V	I	K	E	A	U
HLV	aL	aL	AdV	—	—	—	—	—
3Voy	Voy	—	Voy	Voy	—	—	—	—
ET/2Voy	—	Voy	—	—	Voy	ET	—	—
CE/2Voy	—	—	Voy	—	Voy	—	—	CE
ET/CE/Voy	—	—	—	Voy	—	ET	—	CE
2CE/Voy	—	—	—	—	Voy	—	CE	CE
ET/2CE	—	—	—	—	—	ET	CE	CE
3CE	—	—	—	—	—	CE	CE	CE
3ET	—	—	—	—	—	ET	ET	ET

TABLE II: Composition of the fixed network configurations, shown as stars in the subsequent plots.

CE, each with astrophysical reach shown in Fig. 1) has many potential realizations: the CE and ET detector locations and orientations are as yet undefined, and there are multiple existing 2G facilities which can play the role of the third detector.

For the random network instances in each ensemble, the following procedure is applied to generate a specific set of facilities and detectors. The third-generation facilities (Einstein Telescope and Cosmic Explorer) are allowed to be placed anywhere on the globe with any orientation [16]. The second-generation facilities (i.e., Voyager) are drawn randomly from the five existing or planned second-generation facilities; Hanford, Livingston, Virgo, LIGO India, and Kagra. Any network realization with the detectors placed too close together (area of the triangle spanned by the detectors is less than $0.25 r_\oplus^2$) is rejected. For each class of network we simulate 100 network realizations, except for the case of three Voyagers, for which the total number of three-facility combinations is 10.

In order to highlight likely (or at least plausible) network configurations, for each set of detectors one network configuration is generated from a finite set of facility sites whose coordinates are given in Tab. I. The resulting set of network configurations is given in Tab. II, and in the subsequent plots there networks are shown as stars.

For each network, the resulting SNRs, localizations, and distance uncertainties of the events are calculated. No SNR cuts or trigger thresholds are applied.

A. Localization of neutron-star binaries at $z = 0.3$

Out to redshift $z = 0.3$, one may reasonably expect >500 binary neutron star coalescence events to pass through the earth every year, even assuming a pessimistic merger rate $\sim 100\,\mathrm{Gpc}^{-3}\,\mathrm{yr}^{-1}$. These events, if sufficiently localized, will be within the followup capabilities of next-generation telescopes.

With a network of three separate detector facilities, events can be localized to two ellipses located antipodally on the sky. The degeneracy between the two ellipses can be broken by the inclusion of prior information based on the detectors' antenna patterns. In this work we compute the localization area (90% confidence interval) via the basic Fisher matrix procedure described in Singer and Price [17, §B], with uniform priors.

In Fig. 4 we plot the resulting distributions for the median and best 10% localizations, with the networks sorted by the area spanned by the three detectors. As expected, the localization performance scales inversely with the area. It is also clear that each addition of a 3G detector to the network significantly improves the network's localization capability. A network composed of two 2G detectors and one 3G detector is roughly a factor of 3 better than a baseline set of three 2G detectors. Including two 3G detectors offers and order of magnitude improvement over the baseline, while a full 3G network offers another factor of 4 or 5, with a significant fraction of localizations below 1 deg^2.

In Fig. 5 we plot the best 10% localizations against the median localizations. This result shows that these two metrics are highly correlated, indicating that there is no need to trade

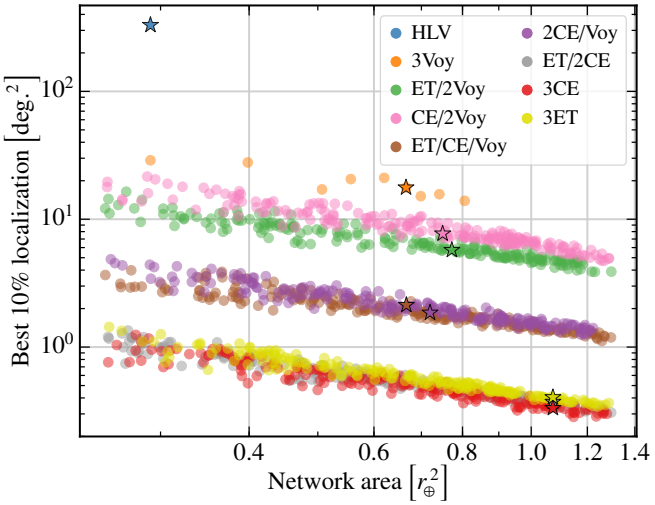

FIG. 4: Distribution of best 10% sky localization areas for randomly simulated networks, shown for $z = 0.3$ and $M_1 = M_2 = 1.4\,M_\odot$. The horizontal axis denotes the area of the triangle spanned by the three detectors in units of earth radii squared.

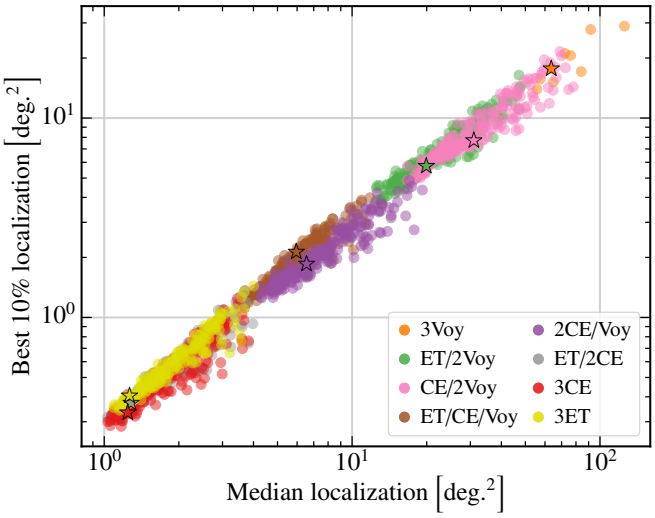

FIG. 5: Scatter plot showing median localization and best 10% localization for $z = 0.3$ and $M_1 = M_2 = 1.4\,M_\odot$. The HLV point is omitted.

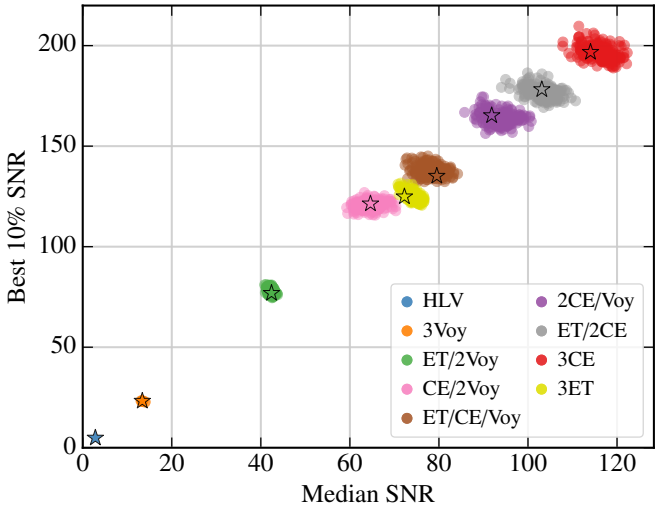

FIG. 6: Scatter plot showing median SNR and best 10% SNR for a $M_1 = M_2 = 30\,M_\odot$ binary black-hole coalescence at redshift $z = 2$.

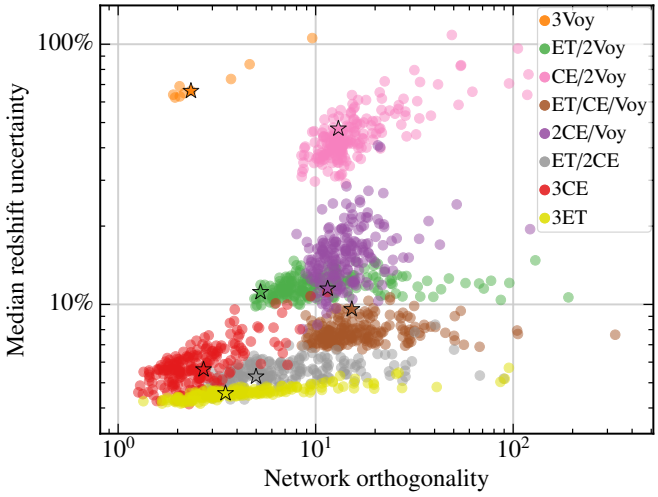

FIG. 7: Distribution of median fractional redshift uncertainties for randomly simulated networks, shown for $z = 2$ and $M_1 = M_2 = 30\,M_\odot$. The horizontal axis denotes the network orthogonality as defined in the text. The HLV point is omitted. **(ME: add 3% pick on y-axis)**

high performance on the best events for good performance on the majority of events, at least for localization capability.

B. Signal-to-noise ratios of black holes at $z = 2$

The distribution of matched-filter network signal-to-noise ratios for a population of 30–30 $M_\odot$ black hole binary coalescences at $z = 2$ is shown in Fig. 6. Unlike the distribution of localizations, the distribution of SNRs has comparatively little dependence on the location and orientation of the detectors; instead, the network performance is determined predominantly by the network composition, with a scatter $\lesssim$30%.

For the networks consisting of two or more third-generation detectors, a slight anticorrelation of the median and best 10% SNRs can be observed. This can be explained as follows: in all cases the network SNR is dominated by the SNR of the third-generation detector(s) (see Fig. 1). For networks with only one third-generation detector, the network SNR is therefore determined by the antenna pattern of the single third-generation detector regardless of its location and orientation. For networks with two or three third-generation detectors, if these detectors are placed so that their antenna patterns mostly overlap, they will jointly detect events at the antenna pattern maxima with good SNR at the expense of events that are incident close to the antenna pattern minima. This leads to enhanced SNR for the best 10% of events and diminished SNR for the median events. Conversely, if these detectors are placed so that their antenna patterns are oriented distinctly, then the network antenna pattern is more isotropic, leading to better SNR for the median events and worse SNR for the best 10% of events.

C. Redshift uncertainties for binary black holes at $z = 2$

Precise measurements of black hole redshifts at $z \gtrsim 1$ can constrain the redshift distribution of black hole binaries, and

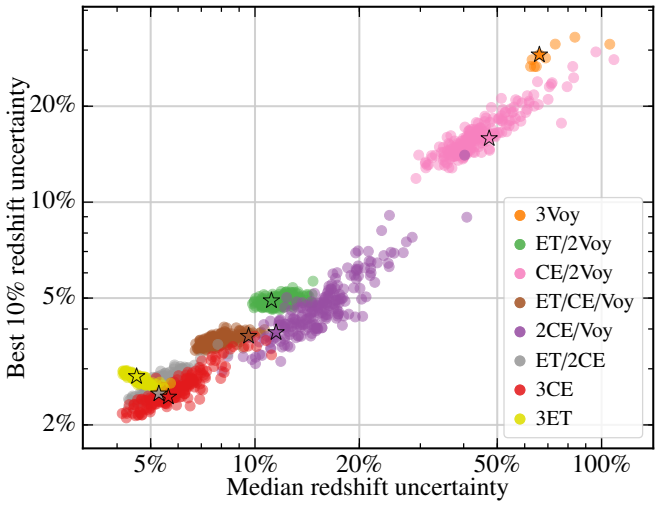

FIG. 8: Scatter plot showing median and best 10% redshift uncertainties for $z = 2$ and $M_1 = M_2 = 30\,M_\odot$. The HLV point is omitted.

hence the star formation rate and the delay time from star formation to merger [18]. Measurement of the redshift is also critical to determining the source-frame mass of the component black holes, thus their astrophysical origin.

Fig. 7 shows the median redshift uncertainties for 30–30 $M_\odot$ black hole binaries coalescing at $z = 2$.

Disentangling the distance (and hence redshift) information from inclination requires good discrimination of the polarization of the incident wave cite.

To quantify the polarization discrimination ability of a particularly network, we can collect the the N detector response tensors, each with five independent components, into an $N \times 5$ matrix and compute its condition number (appendix A).

Fig. 8 shows the median and best 10% redshift uncertainties

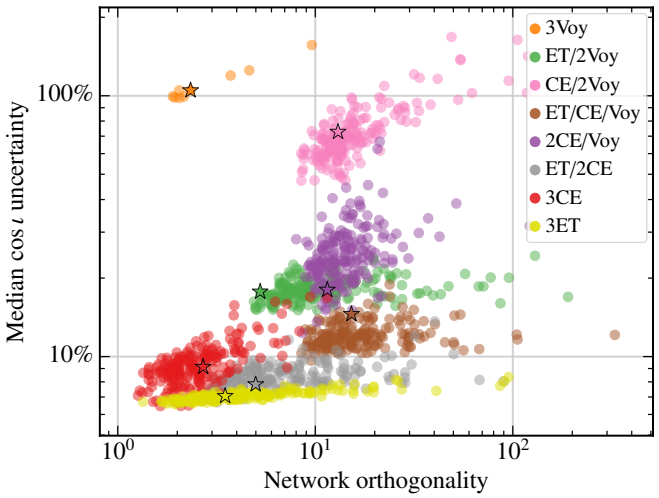

FIG. 9: Distribution of median fractional cos ι uncertainties for randomly simulated networks, shown for $z = 2$ and $M_1 = M_2 = 30\,M_\odot$. The horizontal axis denotes the network orthogonality as defined in the text. The HLV point is omitted.

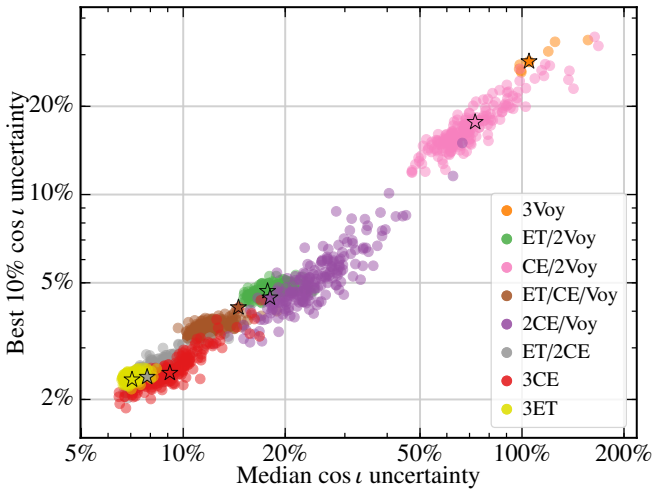

FIG. 10: Scatter plot showing median and best 10% cos ι uncertainties for $z = 2$ and $M_1 = M_2 = 30\,M_\odot$. The HLV point is omitted.

for 30–30 $M_\odot$ black hole binaries coalescing at $z = 2$.

D. Inclination angle uncertainty for black holes at $z = 2$

E. Signal-to-noise ratios at high frequency

Gravitational-wave observations at the kilohertz scale can reveal information about nuclear processes from newly merged neutron stars (the so-called "post-merger" phase of the waveform) [19, 20] and from supernovae [21]. There is considerable uncertainty in the waveforms produced from these events. Therefore, we construct a metric consisting of a uniform strain $h(f) = 1 \times 10^{-25}\,\mathrm{Hz}^{-1}$ from 400 Hz to 4 kHz and zero elsewhere; this frequency range encompasses the frequency spectra

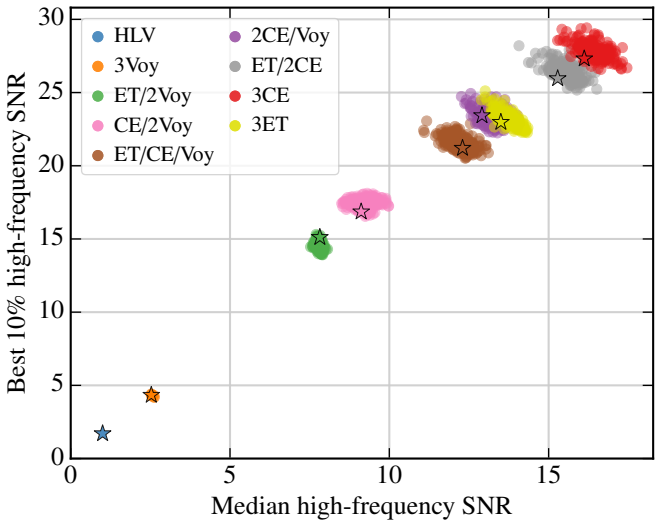

FIG. 11: Median and best 10% high-frequency signal-to-noise ratios for a distribution of 3G networks, assuming a frequency-independent strain $h_0 = 1 \times 10^{-25}$.

predicted from multiple neutron-star post-merger models and supernovae?.

The resulting distributions of signal-to-noise ratios, plotted as median versus best 10%, is shown in Fig. 11. Changing the uniform strain to a frequency-dependent strain $h(f) \propto 1/f^{1/2}$ does not substantively alter the trends shown in Fig. 11. The conclusion from this plot is very similar to that of SNR for binary black hole systems in Fig. 6: while there is an anti-correlation between the best and the median SNR for networks involving 3G detectors, the magnitude of the effect is too small to be a strong driver of network design choices.

IV. DISCUSSION

First, the performance of a three-detector network is determined primarily by its composition, rather than the location and orientation of its detectors. This is particularly evident for the signal-to-noise ratio metrics. For the localization metrics, the network area has a large effect on the performance, but nonetheless this effect is subdominant to the effect of the network composition: the few best networks containing two third-generation instruments are able to outperform only the few worst networks containing three third-generation instruments, for example.

Second, there is not much difference between ranking networks by their median performance or the performance for the best 10% of events. In the signal-to-noise ratio metrics one observes a slight anti-correlation, particularly for networks with two or three third-generation detectors, but this is a $\lesssim$30% effect.

(ME: Say more here!)

Appendix A: Network orthogonality

This appendix describes the network orthogonality parameter described in the main text.

The astrophysical strain incident on a detector network is described by a symmetric, traceless Cartesian tensor of order 2; its matrix representation is

$$\mathsf{H} = \begin{pmatrix} H_{11} & H_{12} & H_{13} \\ H_{12} & H_{22} & H_{23} \\ H_{13} & H_{23} & H_{33} \end{pmatrix}, \tag{A1}$$

with the additional constraint $H_{11} + H_{22} + H_{33} = 0$.

Correspondingly, the response of each detector to H is also a symmetric, tranceless Cartesian tensor of order 2, defined as the difference of the outer products of the detector's arm vectors. Explicitly, for the ith detector in a particular network, the detector tensor is

$$\mathsf{D}^{(i)} = \frac{1}{2}\left[\hat{\mathbf{X}}^{(i)}\hat{\mathbf{X}}^{(i)} - \hat{\mathbf{Y}}^{(i)}\hat{\mathbf{Y}}^{(i)}\right]. \tag{A2}$$

The SNR-weighted strain signal appearing in the ith detector is given by the double contraction of $\mathsf{D}^{(i)}$ and H into a scalar:

$$h^{(1)} = \rho^{(1)}\mathsf{D}^{(1)} : \mathsf{H} \tag{A3a}$$

$$\vdots$$

$$h^{(N)} = \rho^{(N)}\mathsf{D}^{(N)} : \mathsf{H}. \tag{A3b}$$

A symmetric, traceless order-2 tensor in $\mathbb{R}^3$ has five independent components, meaning that both H and the detector tensors can be written in terms of five basis vectors $\mathsf{E}_1, \ldots, \mathsf{E}_5$; [22] the Cartesian matrix representation of one such (orthonormal) basis is

$$\mathsf{E}_1 = \frac{1}{2}\begin{pmatrix} 1 & 0 & 0 \\ 0 & -1 & 0 \\ 0 & 0 & 0 \end{pmatrix} \tag{A4a}$$

$$\mathsf{E}_2 = \sqrt{\frac{2}{3}}\begin{pmatrix} \frac{1}{2} & 0 & 0 \\ 0 & \frac{1}{2} & 0 \\ 0 & 0 & -1 \end{pmatrix} \tag{A4b}$$

$$\mathsf{E}_3 = \frac{1}{2}\begin{pmatrix} 0 & 1 & 0 \\ 1 & 0 & 0 \\ 0 & 0 & 0 \end{pmatrix} \tag{A4c}$$

$$\mathsf{E}_4 = \frac{1}{2}\begin{pmatrix} 0 & 0 & 1 \\ 0 & 0 & 0 \\ 1 & 0 & 0 \end{pmatrix} \tag{A4d}$$

$$\mathsf{E}_5 = \frac{1}{2}\begin{pmatrix} 0 & 0 & 0 \\ 0 & 0 & 1 \\ 0 & 1 & 0 \end{pmatrix} \tag{A4e}$$

With this representation, the system of equations (A3) can instead be written as a matrix equation

$$h^{(i)} = M^{(ij)}H^{(j)}, \tag{A5}$$

where $H^{(j)} = \mathsf{H} : \mathsf{E}^{(j)}$ are the elements of a 5-element column vector, and $M^{(ij)} = \rho^{(i)}\mathsf{D}^{(i)} : \mathsf{E}^{(j)}$ are the elements of an $N \times 5$ matrix $\mathcal{M}$.

The network orthogonality is then defined as the ratio of the largest to smallest nonzero singular values of $\mathcal{M}$:

$$\kappa(\mathcal{M}) = \frac{\max\{\sigma_{>0}(\mathcal{M})\}}{\min\{\sigma_{>0}(\mathcal{M})\}}, \tag{A6}$$

which coincides with the standard definition of matrix condition number if all of the singular values of $\mathcal{M}$ are nonzero.

ACKNOWLEDGMENTS

EDH is supported by the MathWorks, Inc.

[1] B. P. Abbott *et al.* (Virgo, LIGO Scientific), Phys. Rev. Lett. **116**, 061102 (2016), arXiv:1602.03837 [gr-qc].

[2] M. Abernathy, F. Acernese, P. Ajith, B. Allen, P. Amaro-Seoane, N. Andersson, S. Aoudia, P. Astone, B. Krishnan, L. Barack, *et al.*, "Einstein gravitational wave telescope conceptual design study," http://www.et-gw.eu/index.php/etdsdocument (2011).

[3] B. P. Abbott *et al.* (LIGO Scientific), Class. Quant. Grav. **34**, 044001 (2017), arXiv:1607.08697 [astro-ph.IM].

[4] H. Miao, H. Yang, R. X. Adhikari, and Y. Chen, Class. Quant. Grav. **31**, 165010 (2014), arXiv:1305.3957 [gr-qc].

[5] P. Raffai, L. Gondán, I. S. Heng, N. Kelecsényi, J. Logue, Z. Márka, and S. Márka, Class. Quant. Grav. **30**, 155004 (2013), arXiv:1301.3939 [astro-ph.IM].

[6] Y.-M. Hu, P. Raffai, L. Gondán, I. S. Heng, N. Kelecsényi, M. Hendry, Z. Márka, and S. Márka, Class. Quant. Grav. **32**, 105010 (2015), arXiv:1409.2875 [astro-ph.IM].

[7] Y. Michimura, K. Komori, A. Nishizawa, H. Takeda, K. Nagano, Y. Enomoto, K. Hayama, K. Somiya, and M. Ando, Phys. Rev. **D97**, 122003 (2018), arXiv:1804.09894 [gr-qc].

[8] Y. Aso, Y. Michimura, K. Somiya, M. Ando, O. Miyakawa, T. Sekiguchi, D. Tatsumi, and H. Yamamoto (KAGRA), Phys. Rev. **D88**, 043007 (2013), arXiv:1306.6747 [gr-qc].

[9] C. Mills, V. Tiwari, and S. Fairhurst, Phys. Rev. **D97**, 104064 (2018), arXiv:1708.00806 [gr-qc].

[10] S. Vitale and M. Evans, Phys. Rev. **D95**, 064052 (2017), arXiv:1610.06917 [gr-qc].

[11] S. Vitale and C. Whittle, Phys. Rev. **D98**, 024029 (2018), arXiv:1804.07866 [gr-qc].

[12] J. Miller, *Inspiral range with cosmology*, Tech. Rep. T1500491

(LIGO, 2015).
[13] G. M. Harry (LIGO Scientific), *Gravitational waves. Proceedings, 8th Edoardo Amaldi Conference, Amaldi 8, New York, USA, June 22-26, 2009*, Class. Quant. Grav. **27**, 084006 (2010).
[14] R. X. Adhikari, N. Smith, A. Brooks, L. Barsotti, B. Shapiro, B. Lantz, D. McClelland, E. K. Gustafson, D. V. Martynov, V. Mitrofanov, *et al.*, "Ligo voyager upgrade: Design concept," (2018).
[15] J. Abadie *et al.* (VIRGO, LIGO Scientific), (2012), arXiv:1203.2674 [gr-qc].
[16] We do not take into account likely geographical constraints such as oceans. This results in some highly improbable networks, but it means that our exploration of network topology is exhaustive: one should *not* expect to find a geographically forbidden network that vastly outperforms the geographically realistic ones.
[17] L. P. Singer and L. R. Price, Phys. Rev. **D93**, 024013 (2016), arXiv:1508.03634 [gr-qc].
[18] S. Vitale and W. M. Farr, (2018), arXiv:1808.00901 [astro-ph.HE].
[19] J. A. Clark, A. Bauswein, N. Stergioulas, and D. Shoemaker, Class. Quant. Grav. **33**, 085003 (2016), arXiv:1509.08522 [astro-ph.HE].
[20] K. Chatziioannou, J. A. Clark, A. Bauswein, M. Millhouse, T. B. Littenberg, and N. Cornish, Phys. Rev. **D96**, 124035 (2017), arXiv:1711.00040 [gr-qc].
[21] S. E. Gossan, P. Sutton, A. Stuver, M. Zanolin, K. Gill, and C. D. Ott, Phys. Rev. **D93**, 042002 (2016), arXiv:1511.02836 [astro-ph.HE].
[22] Note, however, that a strain tensor produced by a single source on the sky in fact has only four independent components—the sky locations θ and ϕ, and the plus- and cross-polarization amplitudes h_+ and $h_\times$ [23]. Similarly, a detector with two equal-length arms also only has four independent components, two angles θ_X and ϕ_X to describe the orientation of the X arm and θ_Y and ϕ_Y for the Y arm.
[23] Y. Guersel and M. Tinto, Phys. Rev. **D40**, 3884 (1989).